Int. J. Electrochem. Sci., 12 **(2017)** 12037 – 12046, doi: 10.20964/2017.12.01

International Journal of
ELECTROCHEMICAL
SCIENCE
www.electrochemsci.org

Short Communication

Effects of Aluminium Addition on the Oxide Film Formed on 304 Stainless Steel in the Simulated Primary Circuit of the PWR

*Shenghan Zhang, Xiaofang Song**, *Kegang Zhang, Qingxiao Hua, Yu Tan*

School of Environmental Science & Engineering, North China Electric Power University, Baoding 071003, Hebei Province, P. R. China
*E-mail: wantong1998@163.com

Received: 6 June 2017 / *Accepted:* 18 September 2017 / *Published:* 12 November 2017

Aluminium (Al^{3+}) addition in the simulated primary circuit of the pressurized water reactor (PWR) was investigated based on its effect on the oxide film formed on 304 stainless steel (SS). SEM images showed the formation of more compact oxide films after Al^{3+} addition. Deposition of cobalt was inhibited by Al^{3+} addition according to the results from EDX and XPS. Potentiodynamic polarization analysis demonstrated that the corrosion potential of the oxide films observably increased and that the corrosion current density remarkably decreased after Al^{3+} addition. Mott-Schottky plots showed that the semiconductor properties of the oxide films could be changed by Al^{3+} addition. These results revealed the composition and structure changes of the oxide films that resulted in corrosion inhibition of 304 SS and prevention of the radiation field build-up of Co^{2+} in the simulated primary circuit of the PWR. The current work offers a good solution for corrosion and radiation build-up of structural materials in many nuclear plants.

Keywords: Aluminium addition, 304 Stainless steel, Pressurized water reactor, Oxide film.

1. INTRODUCTION

Austenitic stainless steel (SS) has been widely applied as a structural material in water-cooled nuclear reactors due to its excellent corrosion resistance in high-temperature water. Stress corrosion cracking [1-6] and radiation build-up [7-9] of austenitic SS are the main problems that threaten the operational safety of nuclear plants. Deposition of radioactive corrosion products on the out-of-core components causes radiation field build-up [10]. Cobalt (^{60}Co) is known as the primary cause of radiation build-up and can also aggravate the corrosion of material [9]. Zinc (Zn) addition is one effective measure for these problems [11-15]. However, ^{64}Zn in natural zinc might be activated to ^{65}Zn in the primary coolant by the ^{64}Zn (n,γ) ^{65}Zn reaction. ^{65}Zn radionuclide is a γ-irradiator with energies of 1.115 and 0.511 MeV and a half-decay period of $t_{1/2}$= 244.06 d, which can result in aggravation of radiation build-up. Therefore, depleted zinc acetate dehydrate is injected into the primary coolant of the pressurized water reactor (PWR).

Depleted zinc is produced by isotope separation techniques and is highly expensive. Honda et al. [16,17] tested the feasibility of aluminium (Al^{3+}) addition as an alternative to Zn addition because none of the natural Al isotopes result in radiation field build-up in the PWR primary coolant. These researchers found that the corrosion of 304 SS and deposition of ^{60}Co could be suppressed by the addition of 5 ppb Al^{3+} in high-temperature water, according to the mass gain test and component analysis. As such, the data are still scarce on the effects of Al^{3+} addition on the radiation build-up and corrosion behaviour of austenitic SS in the simulated primary circuit of the PWR. More detailed work is needed to reveal the effects of Al^{3+} addition on the formation of oxide film on austenitic stainless steel in high-temperature water.

The current study aimed to investigate the performance of Al^{3+} addition on the oxide film formed on 304 SS. The electrochemical behaviours, semiconductor properties, surface morphology and compositions of the oxide films were analysed in this paper. This work offers a new solution for the control of radiation build-up and corrosion of 304 SS in nuclear plants.

2. EXPERIMENTAL

2.1. Materials

The chemical composition (mass, %) of the 304 SS used in the current work was 0.01 C, 0.63 Si, 1.10 Mn, 8.06 Ni, 19.57 Cr and balance Fe. The 304 SS specimens (12 mm ×10 mm × 2 mm) were gradually ground with SiC papers up to 2000-grit and mechanically polished with alumina gel (0.5 μm). The specimens were ultrasonically cleaned with ethanol and pure water sequentially.

2.2. Exposure tests

Test specimens were exposed in the simulated primary water circuit of the PWR contained in a 1 L autoclave at 553.15 K for 7 d. The simulated solutions were de-aerated by continuous bubbling with nitrogen gas for 2 h prior to the exposure tests. Details of the oxide films formed on 304 SS specimens and the test solutions used in the exposure tests are listed in Table 1. The aqueous solution contained 1200 ppm H_3BO_3 (counted as B), and 2.2 ppm $LiOH\cdot H_2O$ (counted as Li) was prepared as the blank solution. Al^{3+}-free solutions were prepared by adding a certain amount of cobaltous acetate tetrahydrate ($(CH_3COO)_2Co\cdot 4H_2O$, counted as Co, ^{59}Co instead of ^{60}Co) into the blank solution. Al^{3+}-containing solutions were prepared by adding a certain amount of aluminium acetate ($(CH_3COO)_3Al$, counted as Al) into the previous Al^{3+}-free solutions. Test specimens used in morphology and structural analysis were exposed in the blank solution, Al^{3+}-free solution (containing 2 ppm Co^{2+}) and Al^{3+}-containing solutions with 10, 100, and 1000 ppb Al^{3+} additions (2 ppm Co^{2+} contained). Potentiodynamic polarization and Mott-Schottky analyses of the oxide film were performed using specimens exposed in the blank solution, Al^{3+}-free solution (10 ppb Co^{2+} contained) and Al^{3+}-containing solutions with 40, 80, and 120 ppb Al^{3+} additions (10 ppb Co^{2+} contained). Although the 80 ppb upper limit of Al^{3+} is recommended by the Electric Power Research Institute (EPRI) [18], Brobst et al. suggested that the deposition of aluminium silicate could be avoided for concentrations below 200 ppb [19]. To accelerate the reaction process, Al^{3+}-containing solutions with concentrations greater than 80 ppb were also used in the exposure tests.

Table 1. Specimens, oxide films and test solutions used in the exposure tests.

Specimen	Oxide film	Test solution	Usage
Blank	OF_{bl}	1000 ppm BO^{3-},3+2.2 ppm Li^{+}	
Al^{3+}-free	$OF_{Co,2000}$	1000 ppm BO^{3-},3+2.2 ppm Li^{+}+2 ppm Co^{2+}	Morphology and structural analysis
Al^{3+}-containing	$OF_{Al,10}$	1000 ppm BO^{3-},3+2.2 ppm Li^{+}+2 ppm Co^{2+}+10 ppb Al^{3+}	
Al^{3+}-containing	$OF_{Al,100}$	1000 ppm BO^{3-},3+2.2 ppm Li^{+}+2 ppm Co^{2+}+100 ppb Al^{3+}	
Al^{3+}-containing	$OF_{Al,1000}$	1000 ppm BO^{3-},3+2.2 ppm Li^{+}+2 ppm Co^{2+}+1000 ppb Al^{3+}	
Al^{3+}-free	$OF_{Co,10}$	1000 ppm BO^{3-},3+2.2 ppm Li^{+}+10 ppb Co^{2+}	Potentiodynamic polarization and Mott-Schottky analysis
Al^{3+}-containing	$OF_{Al,40}$	1000 ppm BO^{3-},3+2.2 ppm Li^{+}+10 ppb Co^{2+}+40 ppb Al^{3+}	
Al^{3+}-containing	$OF_{Al,80}$	1000 ppm BO^{3-},3+2.2 ppm Li^{+}+10 ppb Co^{2+}+80 ppb Al^{3+}	
Al^{3+}-containing	$OF_{Al,120}$	1000 ppm BO^{3-},3+2.2 ppm Li^{+}+10 ppb Co^{2+}+120 ppb Al^{3+}	

2.3. Characteristic analysis of oxide films

Scanning electron microscopy (SEM, Hitachi S4800, Japan) with energy dispersive X-ray spectroscopy (EDX), X-ray photoelectron spectroscopy (XPS) and electrochemical measurements were used to characterize the oxidized surfaces of the specimens after the high-temperature exposure tests described in Section 2.2. XPS analyses were performed using a PHI Quantera (Japan) instrument with an Al monochromator. The binding energy was calibrated by C 1 s at 284.8 eV. The depth profile information was obtained by argon ion sputtering with a rate of 10 $nm \cdot min^{-1}$ (vs. SiO_2). Potentiodynamic polarization and Mott-Schottky plots were obtained using a three-electrode cell with a platinum counter-electrode and a saturated calomel reference electrode (, all potential values mentioned refer to SCE). The exposed specimens were used as the working electrode with an area of

0.2826 cm^2. Fresh specimens were used in each electrochemical experiment. All measurements were performed at room temperature in borate buffer solutions (0.15 mol·L^{-1} boric acid, 0.0375 mol·L^{-1} sodium borate, and pH 8.4) with a Parstat 2273 (USA) instrument. The potentiodynamic polarization experiments were performed at a scan rate of 1 mV·s^{-1}. The Mott-Schottky experiments were performed by sweeping the potentials in the negative direction with 10 mV intervals and at 1 KHz.

3. RESULTS AND DISCUSSION

3.1. SEM/EDX morphology and composition of the oxide film

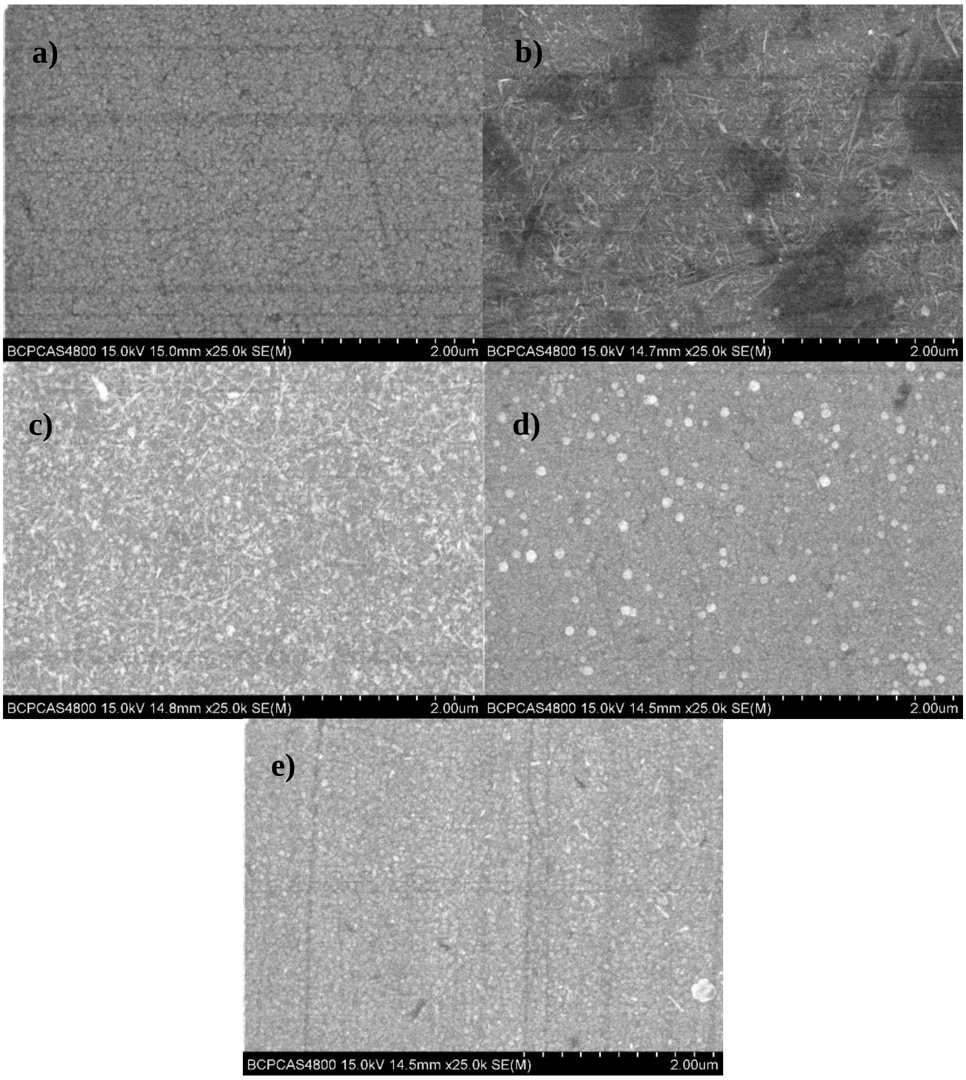

Figure 1. SEM (25000×) images of the oxide films on 304 SS: a) OF_{bl}, b) $OF_{Co,2000}$, c) $OF_{Al,10}$, d) $OF_{Al,100}$ and e) $OF_{Al,1000}$.

The morphology of the oxide film on the 304 SS after the high-temperature exposure test is shown in Fig. 1. The oxide film formed in the blank solution exhibited a uniform coating of polyhedral crystals (Fig. 1a). The oxide film formed in the Al^{3+}-free solution was covered with many needle-like crystals (Fig. 1b). However, the needle-like crystals in the oxide films disappeared gradually with increasing Al^{3+} addition, and the oxide films became more compact (Fig. 1c-e). When the addition of Al^{3+} exceeded 100 ppb, no needle-like crystals were apparent, i.e., the cobalt oxide was reduced, and the oxide particle size was smaller than that formed in the blank solution.

Table 2 shows the EDX results of the oxide films detected by SEM. The atomic percentage (at. %) of Co in the oxide films was reduced with increasing Al^{3+} addition. This result indicated that Al^{3+} addition was capable of retarding the deposition of Co on the surface of 304 SS. ^{60}Co has been identified as the primary cause of radiation build-up [9]. Therefore, Al^{3+} addition undoubtedly can reduce the radiation build-up in the PWR. In addition, the retardation of Co deposition restrained the formation of needle-like crystals on the surface of the oxide film, which increased the compactness of the oxide films and enhanced their corrosion resistance. These results indicated that the oxide film composition and structure could be changed by Al^{3+} addition, which affected the diffusivity of the point defects throughout the oxide film.

Table 2. EDX results (area scanning) of the oxide films formed on 304 SS after exposure in the simulated primary water circuit of the PWR.

Oxide film	At. %					
	Fe	Cr	Ni	Co	Al	O
OF_{bl}	57.69	17.66	5.81	n.d.	n.d.	18.84
$OF_{Co,2000}$	56.31	17.32	5.62	1.13	n.d.	19.62
$OF_{Al,10}$	58.55	17.68	5.94	1.12	0.72	15.99
$OF_{Al,100}$	57.09	17.47	5.68	0.96	0.63	18.17
$OF_{Al,1000}$	57.51	16.97	6.12	0.84	1.38	17.18

n.d.; not detected.

3.2. XPS

XPS analysis was performed for the oxide films formed on 304 SS after high-temperature exposure in Al^{3+}-free and Al^{3+}-containing solutions (Fig. 2). The depth profiles of the oxide films were illustrated by the sputtering time. As expected, in addition to oxygen (O), iron (Fe), chromium (Cr), nickel (Ni), and Co detected in the oxide films, Al was also found in the oxide film formed in the Al^{3+}-containing solution (Fig. 2b). Considerable concentrations of Al were found throughout the oxide film formed in the Al^{3+}-containing solution (Fig. 2b). The 8% Al at the outermost surface in the oxide film suggested a deposition layer of mixed Al-Fe oxides. The greatly reduced Co after Al^{3+} addition indicated that the deposition of Co^{2+} was restrained by Al^{3+} addition, which was in accordance with the previous result obtained by EDX. The intersection of the O and Fe curves is usually taken as the depth of the oxide film. Apparently, the thickness of the oxide film formed in the Al^{3+}-containing solution was much thinner than that formed in the Al^{3+}-free solution. This result indicated that the needle-like crystals on the oxide film formed in the Al^{3+}-containing solution were replaced by fine polyhedral crystals due to Al^{3+} addition, resulting in a compact surface.

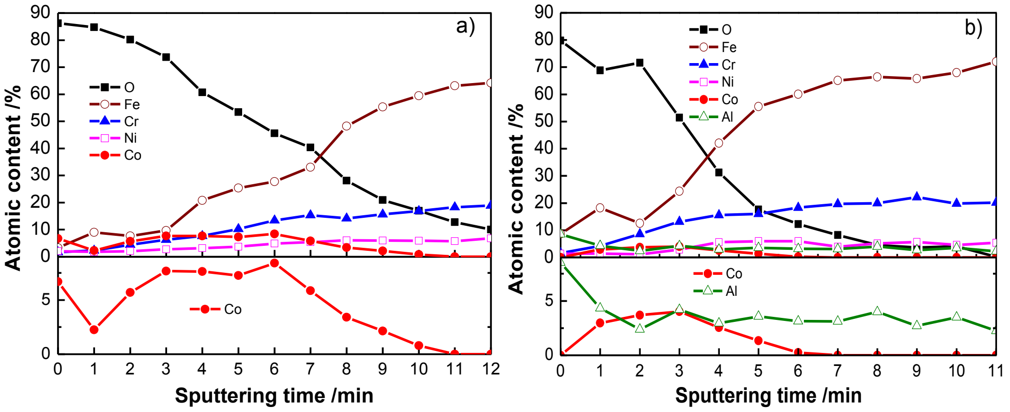

Figure 2. Typical elemental compositions vs. depth profiles (expressed by sputtering time) obtained from XPS for the oxide films on 304 SS: a) $OF_{Co,\ 2000}$ and b) $OF_{Al,\ 100}$.

3.3. Potentiodynamic polarization

The potentiodynamic polarization curves of various oxide films formed on 304 SS after high-temperature exposure were analysed using a three-electrode cell in borate buffer solutions (Fig. 3). The inset figures are plotted and fitted to suggest the Tafel region. The parameters of the electrochemical polarization curves for the oxide films derived from Tafel region extrapolation are listed in Table 3. Passive behaviour was observed in all oxide films after high-temperature exposure in the current work. However, the passive potential range was narrowed compared with the oxide film formed in room-temperature water [20]. The corrosion potential ($\boldsymbol{E_{corr}}$) of the oxide film was shifted slightly towards the negative direction after Co^{2+} addition, whereas the corrosion current density ($\boldsymbol{I_{corr}}$) was increased (Table 3). This result might be attributed to the incorporation of Co^{2+} into the oxide film. The properties of the oxide film were adversely affected by Co^{2+} addition, but the passive potential ranges of the oxide film were similar with and without Co^{2+} addition (-0.3 to 0.2). At the same time, the corrosion potential of the oxide film observably increased and the corrosion current density remarkably decreased after Al^{3+} addition. Additionally, the corrosion current density decreased with the increase in Al^{3+} addition (Table 3). The passive potential range of the oxide film showed no obvious change with and without Al^{3+} addition (-0.2 to 0.3). The inhibition efficiency (IE) is calculated using Eq. 1 [21]:

$$\mathrm{IE} = \frac{i_{corr,Co} - i_{corr,Al}}{i_{corr,Co}} \qquad (1)$$

where $i_{corr,Co}$ and $i_{corr,Al}$ are the corrosion current density of oxide film without and with Al, respectively. The corrosion inhibition of Co^{2+} by Al^{3+} addition was obviously observed in these oxides.

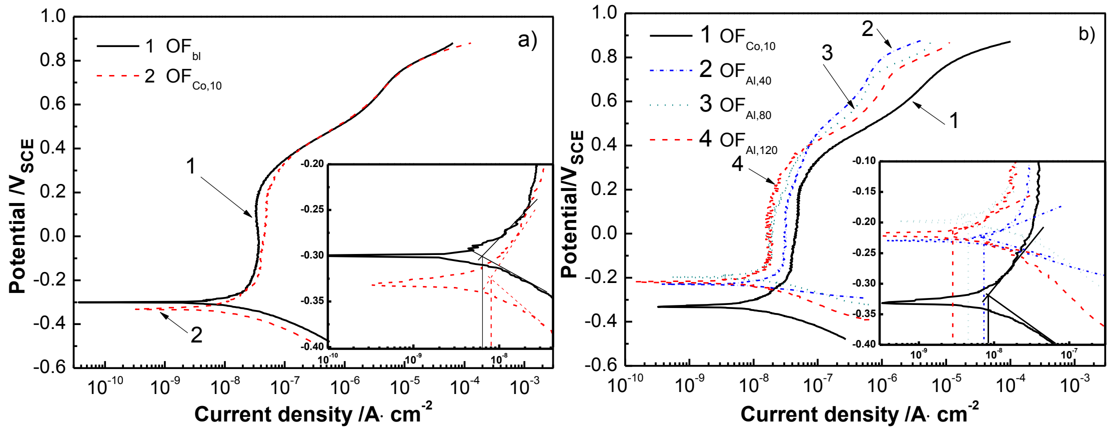

Figure 3. Potentiodynamic polarization plots of the oxide films on 304 SS after high-temperature exposure. a) OF$_{bl}$, OF$_{Co,10}$, b) OF$_{Al,40}$, OF$_{Al,80}$, and OF$_{Al,120}$ (inset: Tafel region with linear fitting).

Table 3. Parameters of electrochemical polarization curves for the oxide films on 304 SS after high-temperature exposure in various solutions.

Oxide film	E_{corr} (mV)	I_{corr} (A·cm^{-2})	b_a (mV·dec^{-1})	b_c (mV·dec^{-1})	IE (%)
OF$_{bl}$	-201.2	6.4×10^{-9}	99.5	55.4	-
OF$_{Co,10}$	-330.8	8.2×10^{-9}	198.6	76.1	-
OF$_{Al,40}$	-227.2	7.3×10^{-9}	83.5	38.9	11.0
OF$_{Al,80}$	-197.5	4.6×10^{-9}	78.3	36.5	43.9
OF$_{Al,120}$	-220.7	2.8×10^{-9}	64.9	33.7	65.8

b_a and b_c are Tafel slopes of the anodic and cathodic Tafel plots.

3.4. Mott-Schottky plots

It is well known that the corrosion performance of an oxide film is correlated with its semiconductor properties. The semiconductor properties of an oxide film can be expressed by the relationship between the space charge region capacitance of the oxide film and the applied potential. If the space charge layer capacitance is less than that of the double layer in the semiconductor/electrolyte interface, the double layer capacitance can be neglected in the capacitance tests. This assumption is reasonable if the frequency is sufficiently high [22-24]. According to the Mott-Schottky theory for an n-type semiconductor, the changes of space charge region capacitance (C) as a function of applied potential (E) can be expressed using Eq. 2 [25-30]:

$$\frac{1}{C^2} = \frac{2}{\varepsilon\varepsilon_0 e N_D}\left(E - E_{fb} - \frac{kT}{e}\right) \qquad (2)$$

where ε is the dielectric constant of the oxide film and, is usually taken as 15.6 [31-33], ε_0 is the vacuum permittivity (8.854×10^{-14} F•cm^{-1}), e is the electron charge (1.602×10^{-19} C), N_D is the donor density for *n*-type semiconductor, E_{fb} is the flat band potential, k is the Boltzmann constant (1.38×10^{-23} J·K^{-1}), T is the absolute temperature, and N_D can be calculated from the slope of the C^{-2} versus E curve.

The Mott-Schottky plots of the oxide films are shown in Fig. 4. The slopes of the curves were positive in the passive potential range (-0.3-0.3 V$_{SCE}$), suggesting *n*-type semiconductor behaviour.

Therefore, the main charge carriers were deemed as oxygen vacancies and cation interstitials according to the point defect model (PDM) [34]. The donor density (N_D) in Fig. 4 was calculated using Eq. 2, and the results are shown in Table 4. The donor densities of the oxide films formed in the Al^{3+}-containing (40 and 80 ppb) solutions were decreased, indicating that the corrosion resistance of the oxide film was enhanced. However, the donor density of oxide film formed in the Al^{3+}-containing (120 ppb) solutions showed little increase, which can be explained by the diffusivity change of the point defect within the film. In addition to the donor density, the growth of oxide film is also controlled by the diffusivity of the point defect within the film [34]. The SEM and XPS analyses demonstrated the composition and structural change of the oxide film formed in the Al^{3+}-containing (100 ppb) solutions that resulted in a change in the diffusion path within the oxide film. Therefore, the diffusivity of the oxide film formed in Al^{3+}-containing (120 ppb) solution dominated the process of oxide film growth.

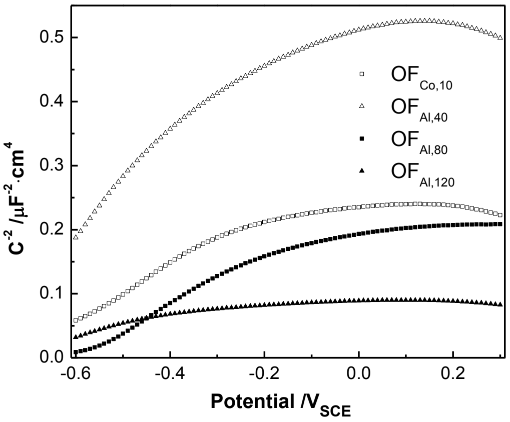

Figure 4. Mott-Schottky plots of the oxide films on 304 SS after high-temperature exposure.

Table 4. Donor density of the oxide films on 304 SS after high-temperature exposure.

	$OF_{Co,10}$	$OF_{Al,40}$	$OF_{Al,80}$	$OF_{Al,120}$
$N_D(cm^3)$	1.36×10^{20}	5.20×10^{19}	7.56×10^{19}	3.40×10^{20}

4. CONCLUSIONS

The oxide films on the surface of 304 SS exposed in the simulated primary circuit of the PWR with or without Al^{3+} addition were investigated using SEM, EDX, and XPS, potentiodynamic polarization, and Mott-Schottky plots. The following conclusions can be drawn based on the results:

1) A more compact oxide film was formed, and the deposition of cobalt was inhibited after Al^{3+} addition, which revealed the structure and composition changes of the oxide films on 304 SS.

2) The corrosion potential of the oxide films observably increased, and the corrosion current density remarkably decreased after Al^{3+} addition.

3) The semiconductor properties of the oxide films were changed by Al^{3+} addition. The donor density within a certain range and the diffusivity of the point defects within the oxide film were both reduced.

4) Al^{3+} addition in the simulated primary circuit of the PWR strengthened the corrosion resistance of 304 SS and inhibited the radiation field build-up of Co^{2+}.

The current work offers a good solution for corrosion and radiation build-up of structural materials in many nuclear plants.

ACKNOWLEDGEMENT
This study was jointly supported by the National Natural Science Foundation of China (9120514015) and the Fundamental Research Funds for the Central Universities (No. 2014 MS122).

References

1. P.M. Scott, P. Combrade, *ASM Handbook*, 13 (2006) 362.
2. H.M. Chung, R.V. Strain, W.J. Shack, *Nucl. Eng. Des*., 208 (2001) 221-234.
3. G.S. Was, P.L. Andresen, *Corrosion*, 63 (2007) 19-45.
4. K.D. Min, S. Hong, D.W. Kim, B.S. Lee, S.J. Kim, *Nucl. Eng. Technol.,* 49(2017)752-759.
5. T.T. Bi, Z.G. Yang, *Eng. Fail. Anal.*, 80 (2017) 453-463.
6. K.X. Liang, Y.F. Xu, W.W. Wang, R.X. Shi, Y. Tan, S.H. Zhang, *Int. J. Electrochem. Sci*., 11 (2016)10928-10938
7. T. Honda, A. Minato, K. Ohsumi, H. Matsubayashi, *C, orrosion*, 43 (1987) 179-185.
8. J. Chêne, F. Martin, *Philos. T. R. Soc. A*, 375 (2017) 20160406.
9. C. C. Lin, *Prog. Nucl. Energ*., 51 (2009) 207-224.
10. L. D. Anstine, EPRI NP-2333 (1982).
11. X. Liu, X. Wu, E.H. Han, *Corros. Sci*., 53 (2011) 3337-3345.
12. Y.L. Guo, E.H. Han, J.Q. Wang, *Mater. Corros*., 66 (2015) 670-680.
13. X. Liu, X. Wu, E. H. Han, *Corros. Sci*., 65 (2012) 136–144.
14. L.F. Zhang, K. Chen, J.M. Wang, X.L. Guo, D.H. Du, P.L. Andresen, *Scripta Mater*., 140 (2017) 50-54.
15. Y. Tan, S.H. Zhang, K.X. Liang, *Int. J. Electrochem. Sci,,,* 9(2014)728-735.
16. T. Honda, K. Ohashi, Y. Furutani, A. Minato, *Corrosion*, 43 (1987) 564-570.
17. T. Honda, M. Izumiya, H. Matsubayashi, K. Ohsumi, H. Matsubayashi, *Nucl. Technol*., 64 (1984) 35-42.
18. PWR Primary Water Chemistry Guidelines Committee, EPRI TR-105714 (1995)
19. G.E. Brobst, S. Stern, EPRI TR-107992 (1997).
20. H. Sun, X.Q. Wu, E.H. Han, *Corros. Sci*., 51 (2009) 2840-2847
21. F. Wedian, M.A. Al-Qudah, G.M. Al-Mazaideh, Int. J. Electrochem. Sci, 12(2017)4664-4676
22. M.C.K Sellers, E.G. Seebauer, *Thin Solid Films*, 519 (2011) 2103-2110.
23. J.L. Lv, T.X. Liang, H, .Y. Luo, *Nucl. En. Des*., 309 (2016) 1-7.
24. M. BenSalah, R. Sabot, E. Triki, L. Dhouibi, P. Refait, M. Jeannin, *Corros. Sci*., 86 (2014) 61-70.
25. W.P. Gomes, D.Vanmaekelbergh, *Electrochim. Acta*, 41 (1996) 967-973.
26. N.E. Hakiki, M.F. Montemor, M.G.S. Ferreira, M.D.C. Belo, *Corros. Sci*., 42 (2000) 687–702.
27. R. Babić, M. Metikoš-Huković, *J. Electroanal. Chem*., 358 (1993) 143–160.
28. M.G.S. Ferreira, N.E. Hakiki, G. Goodlet, S. Faty, A.M.P. Simões, M.D.C. Belo, *Electrochim. Acta.*, 46 (2001)3767–3776.
29. D.G. Li, D.R. Chen, J.D. Wang, P. Liang, *Electrochim. Acta*, 207 (2016) 152-163.

30. P. Muret, A. Traoré, A. Maréchal, D. Eon, J. Pernot, J.C. Pinẽro, M.P. Villar, D. Araujo, *J. Appl. Phys.*, 118 (2015) 204505.
31. Y.X. Qiao, Y.G. Zheng, W. Ke, P.C. Okafor, *Corros. Sci.*, 51 (2009) 979–986.
32. Y. Yang, L. Guo, H. Liu, *J. Power Sources*, 195 (2010) 5651–5659.
33. N. Li, Y. Li, S. Wang, F. Wang, *Electrochim. Acta,* 52 (2006) 760–765.
34. D.D. Macdonald, *Electrochim. Acta*, 56 (2011) 1761-1772.